Search for photon oscillations into massive particles

M. Fouché,* C. Robilliard, S. Faure, and C. Rizzo

Laboratoire Collisions Agrégats Réactivité, IRSAMC, UPS/CNRS, UMR 5589, 31062 Toulouse, France

J. Mauchain, M. Nardone, and R. Battesti

Laboratoire National des Champs Magnétiques Pulsés, CNRS/INSA/UPS, UMR 5147, 31400 Toulouse, France

L. Martin, A.-M. Sautivet, J.-L. Paillard, and F. Amiranoff

Laboratoire pour l'Utilisation des Lasers Intenses, CNRS-CEA-X-Paris VI, UMR 7605, 91128 Palaiseau, France

Recently, axionlike particle search has received renewed interest, and several groups have started experiments. In this paper, we present the final results of our experiment on photon-axion oscillations in the presence of a magnetic field, which took place at the Laboratoire pour l'Utilisation des Lasers Intenses, Palaiseau, France. Our null measurement allowed us to exclude the existence of axions with inverse coupling constant $M > 9. \times 10^5$ GeV for low axion masses and to improve the preceding Brookhaven-Fermilab-Rochester-Trieste (BFRT) Collaboration limits by a factor of 3 or more for axion masses $1.1 < m_a < 2.6$ meV. We also show that our experimental results improve the existing limits on the parameters of a low mass hidden-sector boson usually dubbed "paraphoton" because of its similarity with the usual photon. We detail our apparatus which is based on the "light shining through the wall" technique. We compare our results to other existing ones.

PACS numbers: 12.20.Fv, 14.80.−j

I. INTRODUCTION

Ever since the standard model was built, various theories have been proposed to go beyond it. Many of these involve, if not imply for the sake of consistency, some light, neutral, spinless particles very weakly coupled to standard model particles, and hence difficult to detect.

One famous particle beyond the standard model is the axion. Proposed more than 30 years ago to solve the strong *CP* problem [1,2], this neutral, spinless, pseudoscalar particle has not been detected yet, in spite of constant experimental efforts [3–6]. Whereas the most sensitive experiments aim at detecting axions of solar or cosmic origin, laboratory experiments including the axion source do not depend on models of the incoming axion flux. Because the axion is not coupled to a single photon but to a two-photon vertex, axion-photon conversion requires an external electric or—preferentially—magnetic field to provide for a virtual second photon [7].

At present, purely terrestrial experiments are built according to two main schemes. The first one, proposed in 1979 by Iacopini and Zavattini [8], aims at measuring the ellipticity induced on a linearly polarized laser beam by the presence of a transverse magnetic field, but is also sensitive to the ellipticity and, slightly modified, to the dichroism induced by the coupling of low mass, neutral, spinless bosons with laser beam photons and the magnetic field [9]. The second popular experimental scheme, named "light shining through the wall" [10], consists of first converting incoming photons into axions in a transverse magnetic field, then blocking the remaining photonic beam with an opaque wall. Behind this wall with which the axions do not interact, a second magnetic field region allows the axions to convert back into photons with the same frequency as the incoming ones. Counting these regenerated photons, one can calculate the axion-photon coupling or put some limits on it. This setup was first realized by the BFRT Collaboration in 1993 [3].

Because of their impressive precision, optical experiments relying on couplings between photons and these hidden-sector particles seem most promising. Thanks to such couplings, the initial photons oscillate into the massive particle to be detected. The strength of optical experiments lies in the huge accessible dynamical range: from more than 10^{20} incoming photons, one can be sensitive to 1 regenerated photon.

In fact, the light shining through the wall experiment also yields some valuable information on another hidden-sector hypothetical particle [11]. After the observation of a deviation from a blackbody curve in the cosmic background radiation [12], some theoretical works suggested photon oscillations into a low mass hidden-sector particle as a possible explanation [13]. The supporting model for such a phenomenon is a modified version of electrodynamics proposed in 1982 [14], based on the existence of two U (1) gauge bosons. One of the two can be taken as the usual massless photon, while the second one corresponds to an additional massive particle usually called a paraphoton. Both gauge bosons are coupled, giving rise to photon-paraphoton oscillations. Several years later, more precise observations did not confirm any anomaly in the cosmic background radiation spectrum [15] and the interest for

paraphoton decreased, although its existence was not excluded. More recently, it was found out that similar additional U(1) gauges generally appear in string embeddings of the standard model [16], reviving the interest for experimental limits on the paraphoton parameters [17–19].

Some limits on the mass and the coupling constant of the paraphoton have already been obtained by a photoregeneration experiment [3]. Astrophysical limits on paraphoton parameters also exist. They have been derived from the agreement of the cosmic microwave background with the blackbody radiation [20], and more recently by the absence of distortions in the optical spectrum of distant type Ia supernovae [21].

Our effort was motivated by the observation published by the PVLAS Collaboration, and subsequently retracted [22], which they claimed could be explained by the existence of axions in the mass range 1–2 meV. We have therefore designed an apparatus optimized for that mass region to rapidly prove or disprove the interpretation in terms of axionlike particles of the PVLAS signal. Our preliminary results, excluding at a 3σ confidence level the existence of axions with parameters consistent with the PVLAS observation, have been published in November 2007 [23]. This paper is devoted to the final results of our light shining through the wall experiment, sensitive to axionlike particles and to paraphotons. We first derive the detection probabilities for both particles. We then detail our apparatus whose strength lies in pulsed laser and magnetic fields, thus reducing the demand on the detector noise. Finally, we present our latest experimental results and compare them with the limits obtained by other searches.

II. PHOTOREGENERATION PROBABILITY

A. Axionlike particle

The photon to axionlike particle conversion and reconversion transition probability (in natural units $\hbar = c = 1$, with 1 T $\equiv$ 195 eV^2 and 1 m $\equiv 5 \times 10^6$ eV^{-1}) after propagating over a distance z in the inhomogeneous magnetic field B writes [7,24]

$$p_a(z) = \left| \int_0^z dz' \Delta_M(z') \times \exp(i\Delta_a z') \right|^2, \quad (1)$$

where $\Delta_M = \frac{B}{2M}$ and $\Delta_a = -\frac{m_a^2}{2\omega}$, ω is the photon energy, m_a the axionlike particle mass, and M its inverse coupling constant with two photons. Note that this equation is valid for a light polarization parallel to the magnetic field since the axion has to be a pseudoscalar [1]. Finally, as we have two identical magnets, the photon regeneration probability due to axionlike particles is

$$P_a = p_a^2(L), \quad (2)$$

with L the magnet length.

In order to have a number of regenerated photons as large as possible, the number of incident photons, the detection efficiency, and the integral of the transverse magnetic field over the magnet length L have to be maximized. We define B_0 as the maximum field and L_{eq} as the equivalent length of a magnet producing a uniform magnetic field B_0 such that

$$\int_{-L/2}^{+L/2} B dz = B_0 L_{\text{eq}}. \quad (3)$$

On the other hand, $p_a(z)$ oscillates for too long magnets. Actually, for a homogeneous magnetic field B_0, Eq. (1) gives

$$p_a = \left(\frac{B_0 L}{2M} \right)^2 \frac{\sin^2(\frac{\Delta_{\text{osc}}}{2}L)}{(\frac{\Delta_{\text{osc}}}{2}L)^2}, \quad (4)$$

where $\Delta_{\text{osc}} = -\Delta_a$. In our case, our search was focused on the $1 < m_a < 2$ meV, so that a length larger than 1 m would have been useless.

Finally, very recently a detailed theoretical study of the photon to axionlike particle conversion probability pointed out that an enhancement of this probability is predicted at $m_a = \omega$ [25]. In this particular condition, the probability of getting a photon after the wall is

$$P_a = \frac{3\beta^4}{16qm_a^4} \log\left(\frac{2qm_a^4}{\beta^4} \right), \quad (5)$$

with $\beta = B_0/M$ and $q = \Delta/\omega$ the quality factor of the laser source, and Δ is the laser bandwidth.

B. Paraphoton

In the modified version of electrodynamics developed in 1982 [14], the paraphoton weakly couples with the photon through kinetic mixing. Contrary to axionlike particles, photon-paraphoton oscillations are therefore possible without any external field and are independent of photon polarization.

Recently, the experimental signatures of paraphoton have been discussed in detail in Ref. [19]. The conversion probability of a photon into a paraphoton of mass μ and vice versa after a distance L is given by

$$p_\gamma = 4\chi^2 \sin^2\left(\frac{\mu^2 L}{4\omega} \right), \quad (6)$$

where χ is the photon-paraphoton coupling constant, whose arbitrary value is to be determined experimentally. This equation is valid for a relativistic paraphoton satisfying $\mu \ll \omega$.

Comparing Eqs. (4) and (6), one notes that from a mathematical point of view the two are equivalent, μ corresponding to m_a, and χ to $\frac{B_0 \omega}{M m_a^2}$. This analogy originates from the fact that both formulas describe the same physical phenomenon, i.e., quantum oscillations of a two level

system. Using this mathematical equivalence between paraphoton parameters and axionlike particle parameters, we were able to derive for the enhancement of the paraphoton conversion probability at $\mu = \omega$ a formula equivalent to Eq. (5):

$$P_\gamma = \frac{3\chi^4}{16q} \log\left(\frac{2q}{\chi^4}\right). \tag{7}$$

In the case of a typical photoregeneration experiment, the incoming photons freely propagate for a distance L_1 and might oscillate into paraphotons before being stopped by a wall, after which the paraphotons propagate for a distance L_2 and have a chance to oscillate back into photons that are detected with efficiency η_{det}. The photon regeneration probability due to paraphotons can therefore be written as

$$P_\gamma = p_\gamma(L_1)p_\gamma(L_2) = 16\chi^4\sin^2\left(\frac{\mu^2 L_1}{4\omega}\right)\sin^2\left(\frac{\mu^2 L_2}{4\omega}\right). \tag{8}$$

In our experiment, L_1 is the distance between the focusing lens at the entrance of the vacuum system, which focuses photons but not paraphotons, and the wall, which blocks photons only. Similarly, L_2 represents the distance separating the blind flange just before the regenerating magnet and the lens coupling the renegerated photons into the optical fiber (see Fig. 1).

Note that Eq. (8) is *a priori* valid in the absence of a magnetic field. If a magnetic field is applied, the formula remains valid provided that it can be considered as static during the experiment and its transverse spatial extent is larger than $1/\mu$ [17], which is the case in our experiment for paraphoton masses larger than 2×10^{-5} eV.

III. EXPERIMENTAL SETUP

As shown in Fig. 1, the experimental setup consists of two main parts separated by the wall. An intense laser beam travels through a first magnetic region (generation magnet) where photons might be converted into axionlike particles. The wall blocks every incident photon while axionlike particles would cross it without interacting and may be converted back into photons in a second magnetic
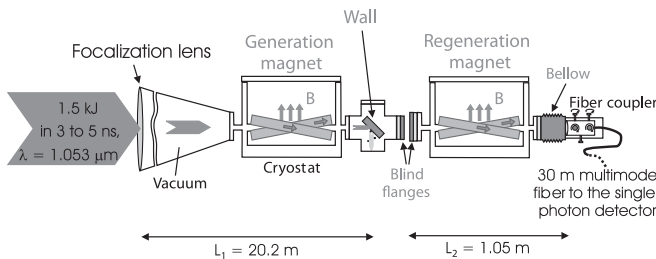
region (regeneration magnet). The regenerated photons are finally detected by a single-photon detector.

The three key elements leading to a high detection rate are the laser, the generation, and regeneration magnets placed on each side of the wall and the single-photon detector. Each element is described in the following sections.

A. Laser

In order to have the maximum number of incident photons at a wavelength that can be efficiently detected, the experiment has been set up at the Laboratoire pour l'Utilisation des Lasers Intenses (LULI) in Palaiseau, on the Nano 2000 chain [26]. It can deliver more than 1.5 kJ over a few nanoseconds with $\omega = 1.17$ eV. This corresponds to $N_i = 8 \times 10^{21}$ photons per pulse.

The nanosecond pulse is generated by a yttrium lithium fluoride seeded oscillator with a $\Delta = 1.7$ meV bandwidth. It delivers 4 mJ with a duration adjustable between 500 ps and 5 ns. Temporal shaping is realized with five Pockels cells. Then this pulse seeds single-pass Nd:pPhosphate glass rods and disk amplifiers. During our 4 weeks of campaign, the total duration was decreased from 5 ns the first week to 4 ns and finally 3 ns while keeping the total energy constant. (A typical time profile is shown in the inset of Fig. 6 with a full width at half maximum of 2.5 ns and a total duration of 4 ns.)

The repetition rate of high energy pulses is imposed by the relaxation time of the thermal load in the amplifiers which implies wave-front distortions. Dynamic wave-front correction is applied by use of an adaptive-optics system [27]. To this end a deformable mirror is included in the middle of the amplification chain. It corrects the spatial phase of the beam to obtain at focus a spot of about once or twice the diffraction limit, as shown in Fig. 2. This system allows one to increase the repetition rate while maintaining good focusability although the amplifiers are not at thermal equilibrium. During data acquisition, the repetition rate has

FIG. 1. Sketch of the apparatus. The wall and the blind flanges are removable for fiber alignment.
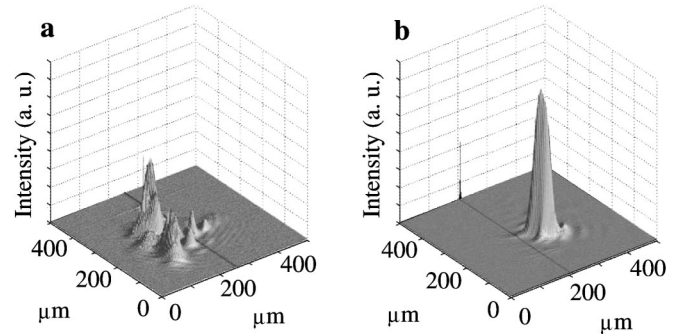
FIG. 2. Focal spot without correction (a) and with wave-front correction (b). This correction allows one to maintain a spot of one or two diffraction limits despite the amplifiers' not being in thermal equilibrium.

typically varied between 1 pulse per hour and 1 pulse every other hour.

At the end of the amplification chain, the vertically linearly polarized incident beam has a 186 mm diameter and is almost perfectly collimated. It is then focused using a lens with focal length 20.4 m. The wall is placed at $L_1 =$ 20.2 m from the lens in order to have the focusing point a few centimeters behind this wall. The beam is well apodized to prevent the incoming light from generating a disturbing plasma on the sides of the vacuum tubes.

Before the wall where the laser beam propagates, a vacuum better than 10^{-3} mbar is necessary in order to avoid air ionization. Two turbo pumps along the vacuum line easily give 10^{-3} mbar near the lens and better than 10^{-4} mbar close to the wall. The wall is made of a 15 mm width aluminum plate to stop every incident photon. It is tilted by 45° with respect to the laser beam axis in order to increase the area of the laser impact and to avoid retroreflected photons. In the second magnetic field region, a vacuum better than 10^{-3} mbar is also maintained.

Figure 3 shows a histogram of laser energy per pulse for the 82 laser pulses performed during our campaign. The laser energy per pulse ranges from 700 J to 2.1 kJ, with a mean value of 1.3 kJ.

B. Magnetic field

Concerning the magnets, we use a pulsed technology. The pulsed magnetic field is produced by a transportable generator developed at LNCMP [28], which consists of a capacitor bank releasing its energy in the coils in a few milliseconds. Besides, a special coil geometry has been developed in order to reach the highest and longest transverse magnetic field. Coil properties are explained in Ref. [29]. Briefly, the basic idea is to get the wires generating the magnetic field as close as possible to the light path. As shown in Fig. 4, the coil consists of two interlaced racetrack shaped windings that are tilted one with respect to the other. This makes room for the necessary optical access at both ends in order to let the laser in while
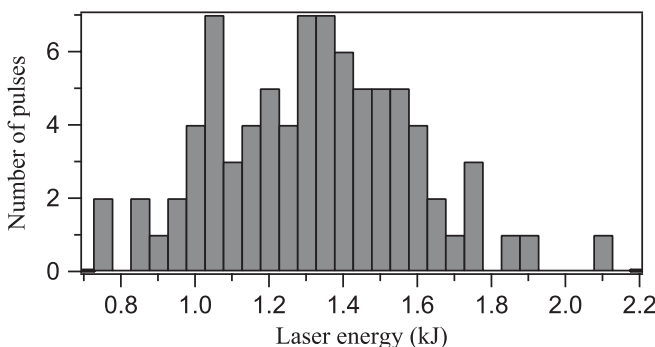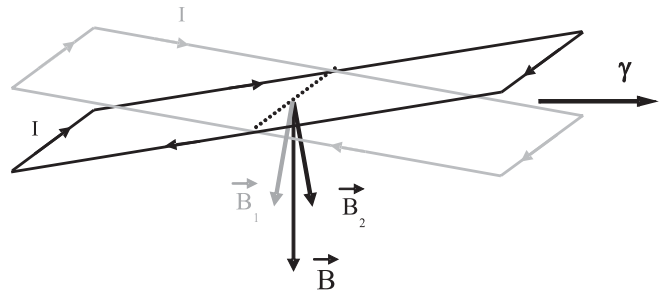

FIG. 4. Scheme of XCoil. Magnetic fields $\vec{B}_1$ and $\vec{B}_2$ are created by each of the racetrack shaped windings. This yields a high transverse magnetic field $\vec{B}$ while allowing the necessary optical access for the laser photons γ.

providing a maximum $B_0 L_{eq}$. Because of the particular arrangement of wires, these magnets are called Xcoils.

The coil frame is made of G10 which is a nonconducting material commonly used in high stress and cryogenic temperature conditions. External reinforcements with the same material have been added after wiring to contain the magnetic pressure that can be as high as 500 MPa. A 12 mm diameter aperture has been dug into the magnets for the light path.

As for usual pulsed magnets, the coils are immersed in a liquid nitrogen cryostat to limit the consequences of heating. The whole cryostat is double walled for a vacuum thermal insulation. This vacuum is in common with the vacuum line and is better than 10^{-4} mbar. A delay between two pulses is necessary for the magnet to cool down to the equilibrium temperature which is monitored via the Xcoils' resistance. Therefore, the repetition rate is set to 5 pulses per hour. Furthermore, the coils' resistance is precisely measured after each pulse and when equilibrium is reached, in order to check the Xcoils' nonembrittlement. Indeed variations of the resistance provide a measurement of the accumulation of defects in the conductor material that occur as a consequence of plastic deformation. These

FIG. 3. Number of high energy pulses versus laser energy during the four weeks of data acquisition.
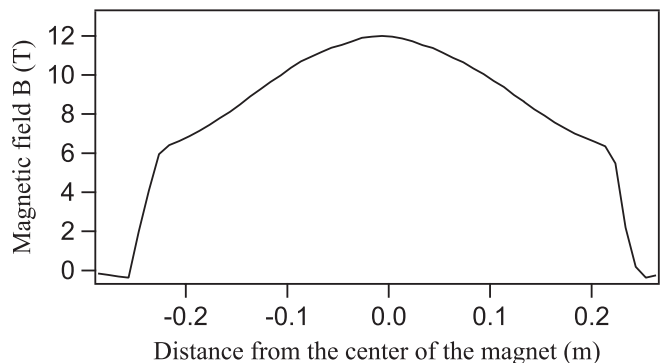

FIG. 5. Transverse magnetic field inside the magnet along the laser direction. At the center of the magnet we have a mean maximum magnetic field $B_0 = 12$ T. Integrating B along the optical path yields 4.38 Tm.

defects lead to hardening and embrittlement of the conductor material, which ultimately leads to failure.

The magnetic field is measured by a calibrated pickup coil. This yields the spatial profile shown in Fig. 5. The maximum field B_0 is obtained at the center of the magnet. Xcoils have provided $B_0 \geq 13.5$ T over an equivalent length $L_{eq} = 365$ mm. However, during the whole campaign a lower magnetic field of $B_0 = 12(0.3)$ T was used to increase the coils' lifetime.

A typical time dependence of the pulsed magnetic field at the center of the magnet is represented in Fig. 6. The total duration is a few milliseconds. The magnetic field reaches its maximum value within less than 2 ms and remains constant ($\pm 0.3\%$) during $\tau_B = 150$ μs, a very long time compared to the laser pulse.

C. Detector

The last key element is the detector that has to meet several criteria. In order to have a sensitivity as good as possible, the regenerated photon detection has to be at the single-photon level. The integration time is limited by the longest duration of the laser pulse which is 5 ns. Since we expected about 100 laser pulses during our four week campaign, which corresponds to a total integration time of 500 ns, we required a detector with a dark count rate [30] far lower than 1 over this integration time, so that any increment of the counting would be unambiguously associated to the detection of one regenerated photon.

Our detector is a commercially available single-photon receiver from Princeton Lightwave which has a high detection efficiency at 1.05 μm. It integrates a 80×80 μm^2 InGaAs avalanche photodiode (APD) with all the necessary bias, control, and counting electronics. Light is coupled to the photodiode through a FC/PC connector and a multimode fiber. When the detector is triggered, the APD bias voltage is raised above its reverse breakdown voltage V_{br} to operate in "Geiger mode." A short time

later—adjustable between 1 and 5 ns—the bias is reduced below V_{br} to avoid false events. For our experiment, the bias pulse width is 5 ns to correspond with the longest laser pulse.

Typical output signals available on the detector are plotted in Fig. 7. Let us first consider Fig. 7(a) with no incident photon. The upper signal corresponds to the amplified APD output. The application of such a short pulse to a reverse-biased APD produces a capacitive transient. The first two transients temporally shifted by 5 ns correspond to the bias pulse. This signal enables one to precisely determine the moment when detection starts. The last transients are due to an electronic reflection of the bias pulse.

When a photon is detected [Fig. 7(b)], the signal resulting from a photon-induced avalanche superimposes upon transients. The transient component may be much larger than the photon-induced component, making it difficult to discern. The detector uses a patented transient cancellation scheme to overcome this problem [31]. A replica of the unwanted transient is created and subtracted from the initial signal. The photon-induced signal will thus appear against a flat, low-noise background, as it is observed in Fig. 7(b) between the initial bias pulse and the reflected one. It can then be easily detected using a discriminator. To this end, this signal is sent to a fast comparator with adjustable threshold that serves as a discriminator and outputs a logic pulse, as shown by lower traces on Fig. 7.

To optimize the dark count rate and the detection efficiency η_{det}, three different parameters can be adjusted: the APD temperature, the discriminator threshold V_d set to
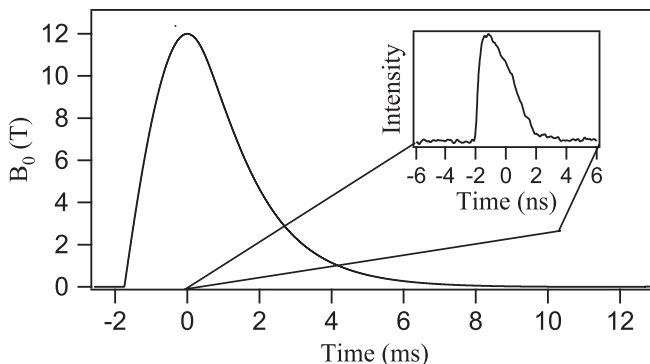

FIG. 6. Magnetic field B_0 at the center of the magnet as a function of time. The maximum is reached within 1.75 ms and can be considered as constant ($\pm 0.3\%$) during $\tau_B = 150$ μs. The 3–5 ns laser pulse is applied during this interval. Inset: temporal profile of a 4 ns laser pulse.
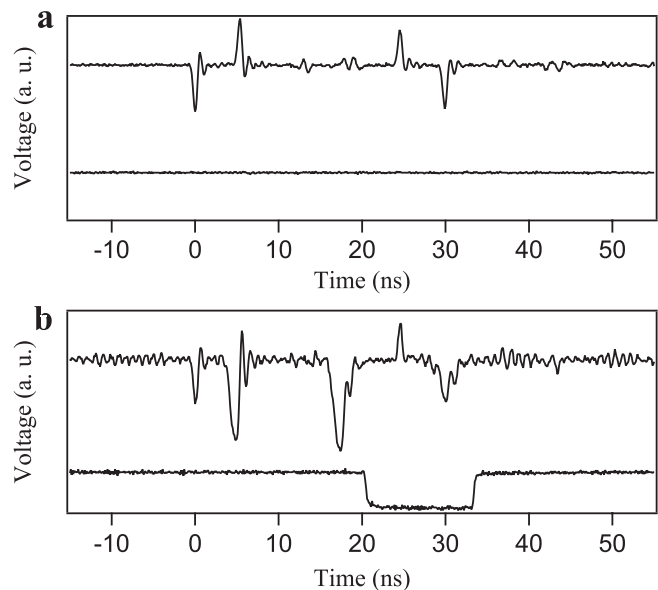

FIG. 7. Amplified APD output (upper curve) and logic signal (lower curve) of the detector as a function of time. The capacitive transients on the APD output signals are due to the gated polarization of the photodiode in Geiger mode. (a) Signals with no incident photon. (b) Signals when a photon is detected.

reject electronic noise, and the APD bias voltage V_{APD}. The dark count rate is first optimized by choosing the lowest achievable temperature which is around 221 K. This rate is measured with no incident light, a trigger frequency of 5 kHz, and an integration time of at least 1 s. Dark counts for a 5 ns detection gate as a function of V_d is shown in Fig. 8(a). It increases rapidly when V_d is too low. On the other hand, η_{det} remains constant for a large range of V_d. We set V_d to a value far from the region where the dark count increases and where η_{det} is still constant. This corresponds to less than 2.5×10^{-2} dark count over 500 ns integration time.

The detection efficiency is precisely measured by illuminating the detector with a laser intensity lower than 0.1 photon per detection gate at 1.05 μm. The probability to have more than one photon per gate is thus negligible. Such a low intensity is obtained with the setup described in Fig. 9. A cw laser is transmitted through two supermirrors with a reflectivity higher than 99.98% [32]. The angle of incidence is near normal in order to intercept the reflected beam and avoid spurious light without increasing transmission. This gives a measured transmission of 0.015% for each mirror. Finally, to calculate the number of incident photons on the detector, we measure the laser power before the two supermirrors with a precise power sensor.

The detection efficiency as a function of the bias voltage is plotted in Fig. 8(b). Our measurements show that η_{det}

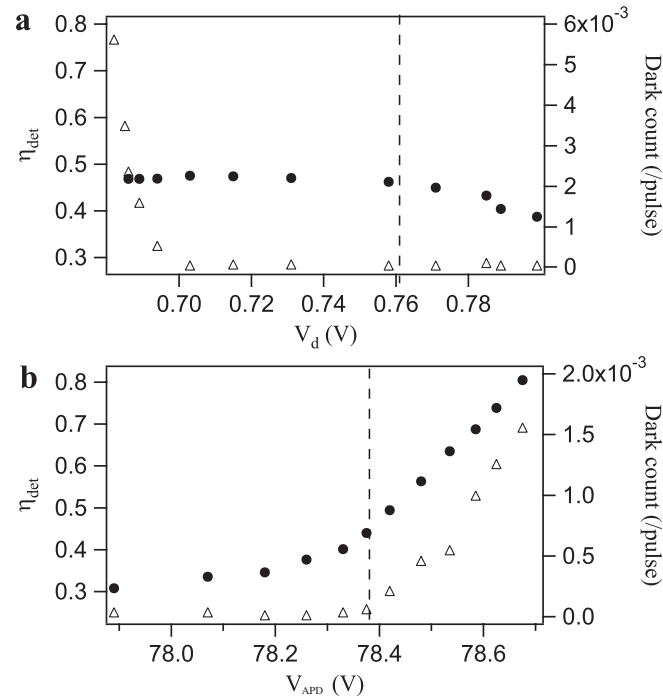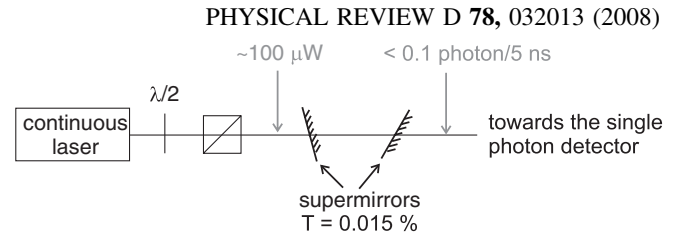FIG. 9. Experimental setup to measure the detection efficiency of the single-photon detector. The detector is illuminated with a laser intensity lower than 0.1 photon per 5 ns. This intensity is calculated through the measurement of the supermirrors transmission and the laser power before those supermirrors. A half wave plate and a polarizer are used to change the number of incident photons.

slowly increases with V_{APD} until a threshold where it increases dramatically for a value of V_{APD} shortly below the dark count runaway value. The best compromise between detection efficiency and dark count rate is found at $V_{APD} = 78.4(0.05)$ V with $\eta_{det} = 0.48(0.025)$.

As mentioned in the Introduction, other similar experiments generally require long integration times which implies an experimental limitation due to the detection noise. Using pulsed laser, magnetic field and detection is an original and efficient way to overcome this problem. Photons are concentrated in very intense short laser pulses during which the detection background is negligible. This also means that if a photon is detected in our experiment in correlation with the magnetic field, it will be an unambiguous signature of axion generation inside our apparatus.

IV. EXPERIMENTAL PROTOCOL AND TESTS

A. Alignment

After the second magnet, the regenerated photons are injected into the detector through a coupling lens and a graded index multimode fiber with a 62.5 μm core diameter, a 0.27 numerical aperture, and an attenuation lower than 1 dB/km. These parameters ensure that we can inject light into the fiber with a high coupling ratio, even when one takes into account the pulse by pulse instability of the propagation axis that can be up to 9 μrad.

Injection is adjusted thanks to the fiber coupler and by removing the wall and the blind flanges (see Fig. 1). As the high energy laser beam, the alignment beam comes from the pilot oscillator without chopping nor amplifying it. This procedure ensures that the pulsed kJ beam is perfectly superimposed to the alignment beam. During data acquisition, the mean coupling efficiency through the fiber was found to be $\eta_c = 0.85$.

The alignment of the high energy beam is performed with a low energy 5 ns pulsed beam, allowing for a 10 Hz repetition rate. During alignment, several black crosses are distributed along the laser path to mark the optical axis. Mirrors mounted on stepper motors allow one to align the beam very precisely on this axis. This procedure is carried out a few minutes before each high energy pulse.

FIG. 8. Detection efficiency (●) and dark count per 5 ns bias pulse (△) as a function of the discriminator threshold (a) (V_{APD} fixed to 78.4 V) or APD bias voltage (b) (V_d fixed to 0.760 V). The APD temperature is fixed to the lowest achievable value 221.5 K. Dashed lines indicate the chosen working point.

The only remaining source of misalignment lies in thermal effects during the high energy pulse, which could slightly deviate the laser beam, hence generating supplementary losses in fiber coupling. This misalignment is mostly reproducible. This means that it can be corrected by a proper offset on the initial laser pointing. The far field of the high energy beam is imaged for each pulse at the output of the amplification chain (see Fig. 10). Since the focal length of the imaging system is similar to that of our focalization lens, the position of the far field image on the alignment mark is a fair diagnosis of the alignment on the fiber coupler. The best offset was determined by a trial and error method after a few high energy pulses.

B. Optical and electromagnetic noise

In order to have the best sensitivity, a perfect optical shielding is necessary. As shown in Fig. 1, an aluminum blind flange closes the entrance to the regeneration magnet. A black soft PVC bellow placed between the exit of the magnet and the fiber coupler prevents stray light while mechanically decoupling the magnet which vibrates during its pulse and the fiber coupler which should stay perfectly still. Finally, another aluminum blind flange closes the exit of the generation area in order to stop any incident photon scattered inside the vacuum line.

A count on the single-photon receiver is most probably due to an incident photon on the photodiode but it may also originate from electromagnetic noise during laser or magnetic pulses. To avoid such noise, the detector is placed in a Faraday shielding bay. In addition, a 30 m long fiber is used so that the detector can be placed far away from the magnets.

To test our protective device, laser and magnetic pulses were separately applied while triggering the detector. No fake signal was detected, validating the optical and electromagnetic shielding.
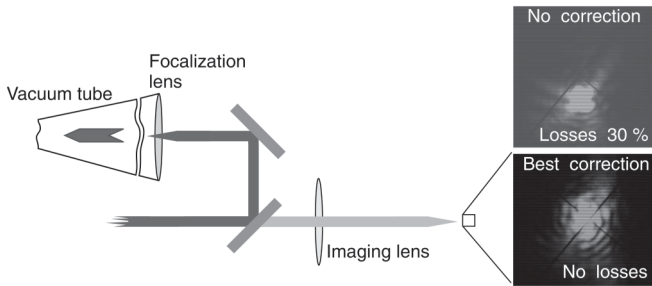

FIG. 10. Monitoring of the optical path followed by the high energy beam. Losses due to misalignment are estimated by comparing the center of the beam to the center of the black cross. The upper image corresponding to an uncorrected laser beam pointing exhibits 30% injection losses, while the lower one is perfectly corrected.
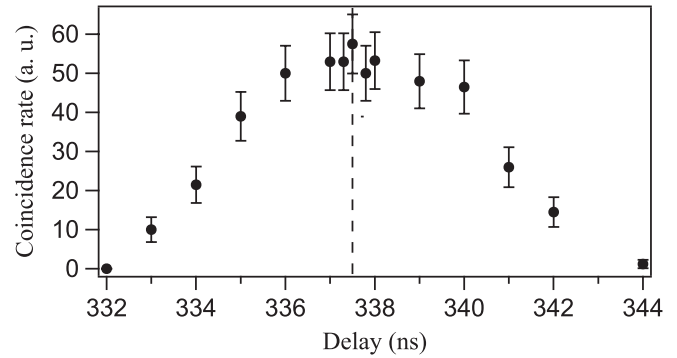

FIG. 11. Coincidence rate between the arrival of photons on the detector and its 5 ns detection gate as a function of an arbitrary delay time. The dashed line indicates our working point, chosen in order to maximize the coincidence rate.

C. Synchronization

Our experiment is based on pulsed elements which require a perfect synchronization: the laser pulse must cross the magnets when the magnetic field is maximum and fall on the photodiode during the detection gate.

The magnetic pulse is triggered with a transistor–transistor logic signal from the laser chain. The delay between this signal and the laser trigger is adjusted once and for all by monitoring on the same oscilloscope the magnetic field and the laser trigger. Then, the magnetic trigger has a jitter lower than 10 μs, ensuring that the laser pulse travels through the magnets within the 150 μs interval during which the magnetic field is constant and maximum.

Synchronization of the laser pulse and the detector needs to be far more accurate since both have a 5 ns duration. The detector gate is triggered with the same fast signal as the laser, using delay lines. We have measured the coincidence rate between the arrival of photons on the detector and the opening of the 5 ns detector gate as a function of an adjustable delay. We have chosen our working point in order to maximize the coincidence rate (see Fig. 11). To perform such a measurement we used the laser pilot beam which was maximally attenuated by shutting off 4 Pockels cells along the amplification chain and chopped with a pulsed duration of 5 ns, which corresponds to the longest duration of the kJ beam.

V. DATA ANALYSIS

A. Detection sensitivity

The best experimental limits are achieved when no fake signal is detected during the experiment. In this case, to estimate the corresponding upper conversion probability of regenerated photons, we have to calculate the upper number of photons that could have been missed by the detector for a given confidence level (CL).

The probability P_n that n incident photons have been missed by the detector is $P_n = (1 - \eta_{\text{det}})^n$ when dark count is negligible. Therefore, the probability that n pho-

tons at most were missed by the detector writes

$$\frac{\sum_{k=0}^{n} P_k}{\sum_{k=0}^{\infty} P_k} = 1 - (1 - \eta_{\text{det}})^{n+1}$$

and has to be compared with the required CL. This yields the upper number of possibly missed photons n_{missed} as the smallest integer n satisfying

$$1 - (1 - \eta_{\text{det}})^{n+1} \geq \text{CL},$$

which writes

$$n_{\text{missed}} = \frac{\log(1 - \text{CL})}{\log(1 - \eta_{\text{det}})} - 1. \quad (9)$$

For example, with our value of η_{det}, a confidence level of 99.7% corresponds to less than eight missed photons. The upper photon regeneration probability is then

$$P_{a \text{ or } \gamma} = \frac{n_{\text{missed}}}{N_{\text{eff}}}, \quad (10)$$

where N_{eff} is the number of effective incident photons over the total number of laser shots, taking into account the losses described hereafter. Our experimental sensitivity limit for the coupling constant versus mass is finally calculated by numerically solving Eqs. (1) and (2) for axionlike particles, and Eqs. (6) and (8) for paraphotons.

B. Photon losses

The number of photons per laser pulse N_i is measured at the end of the amplification chain with a calibrated calorimeter. Then the number of effective incident photons on the detector N_{eff} should take into account every loss. The first source of loss is due to the coupling efficiency through the fiber. This is precisely calibrated once a day. Injection is checked before each pulse, just after the alignment of the high energy beam. The mean coupling efficiency is $\eta_c = 0.85$.

As said before, the main source of misalignment lies in thermal effects during the high energy laser pulse, whose mean value was corrected. Furthermore, using the cw alignment beam we calibrated the injection losses in the fiber as a function of the misalignment visible on the far field imaging. Thanks to this procedure, we were able to estimate the actual alignment losses for each pulse: they amounted to 30% for a noncorrected pulse and varied between 0% and 10% for corrected pulses, because of pulse-to-pulse instabilities.

Possible jitter between the beginning of the detection and the arrival of the laser pulse on the detector is also taken into account. For each pulse, a single oscilloscope acquires the laser trigger and the detector trigger as well as the detection gate. Those curves allow one to precisely calculate the moment t_0 when detection actually starts compared to the laser pulse arrival. Furthermore, the temporal profile of each laser pulse is also monitored. By integrating this signal from t_0 and during the 5 ns of

detection, the fraction η_f of photons inside the detection gate is calculated. This fraction has fluctuated between 0.6 and 1 at the beginning of our data acquisition with the 5 ns pulse, mainly due to a 1 ns jitter that was then reduced to about 200 ps. Then, with the 4 and 3 ns laser pulses, jitter is less critical and $\eta_f = 1$ is obtained almost all the time.

Finally, for axionlike particles the numerical solving of Eq. (1) is performed with a fixed magnetic field B_0. Variations of this magnetic field along data acquisition are taken into account by multiplying each number of incident photons by the factor $(B_{0,i}/B_0)^4$, where $B_{0,i}$ is the maximum field for the ith pulse.

Integration of every loss yields a total number of effective photons

$$N_{\text{eff},a} = \sum_i \eta_{c,i} \eta_{p,i} \eta_{f,i} \left(\frac{B_{0,i}}{B_0}\right)^4 N_i, \quad (11)$$

the sum being taken over the total number of laser and magnetic pulses.

Concerning paraphotons, given that the magnetic fields have no effect on the oscillations, the formula is written as

$$N_{\text{eff},\gamma} = \sum_i \eta_{c,i} \eta_{p,i} \eta_{f,i} N_i. \quad (12)$$

VI. RESULTS

Data acquisition was spread over four different weeks. As shown in Fig. 3, 82 high energy pulses have reached the wall with a total energy of about 110 kJ. This corresponds to 5.9×10^{23} photons. During the whole data acquisition, no signal has been detected.

A. Axionlike particles

The magnetic field was applied during 56 of those laser pulses, with a mean value of 12 T. The laser pulses without magnetic field aimed at testing for possible fake counts.

Our experimental sensitivity limits for axionlike particle at 99.7% confidence level are plotted in Fig. 12. They
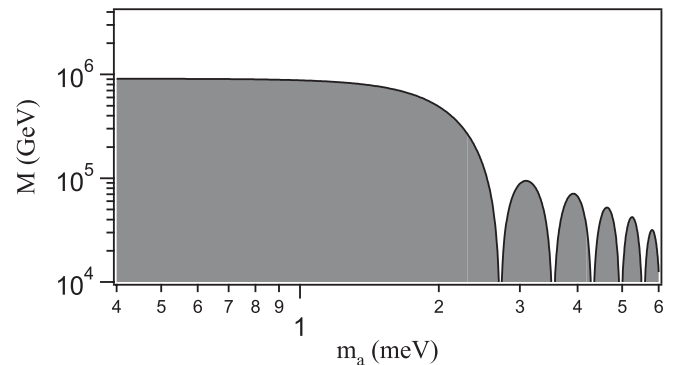
FIG. 12. 3σ limits for the axionlike particle—two-photon inverse coupling constant M, as a function of the axionlike particle mass m_a, obtained from our null result. The area below our curve is excluded.

correspond to a detection probability of regenerated photons $P_a = 3.3 \times 10^{-23}$ and give $M > 9.1 \times 10^5$ GeV at low masses. The dark gray area below our curve is excluded. This improves the limits we have published in [23], which already excluded the PVLAS results [22].

We also compared our limits to other laboratory experiments in Fig. 13. They are comparable to other purely laboratory experiments [3,33,34], especially in the meV region of mass. On the other hand, they are still far from experiments in which limits (stripes) approach models predictions [4,5,35,36].

Using Eq. (5), our experimental results correspond to $M > 8$ GeV at $m_a = 1.17$ eV. Despite this enhancement, our limits are still very far from the inverse coupling constant of model predictions which is around 10^9 GeV for a 1 eV mass.

B. Paraphotons

In the case of paraphotons, we take into account the laser bandwidth Δ by averaging $P_\gamma(\omega)$ over Δ:
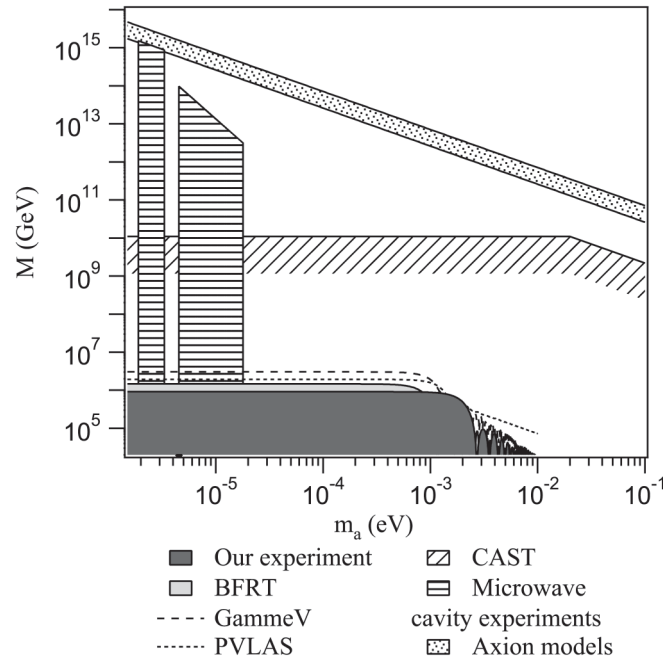

FIG. 13. Limits on the axionlike particle—two-photon inverse coupling constant M as a function of the axionlike particle mass m_a obtained by experimental searches. Our exclusion region is first compared to other purely laboratory experiments such as the BFRT photon regeneration experiment [3], the GammeV experiment [33], and the PVLAS Collaboration [34] with a 3σ confidence level. Those curves are finally compared to the 95% confidence level exclusion region obtained on CAST [5] and the more than 90% confidence level on microwave cavity experiments [4,35,36]. Model predictions are also shown as a dotted stripe between the predictions of the KSVZ model (lower line, $E/N = 0$) [44] and of the DFSZ model (upper line, $E/N = 8/3$) [45].

$$\bar{P}_\gamma = \frac{1}{\Delta} \int_{\omega-(\Delta/2)}^{\omega-(\Delta/2)} P_\gamma(\omega) d\omega. \qquad (13)$$

The experimental sensitivity is then calculated by numerically solving

$$\bar{P}_\gamma = \frac{n_{\text{missed}}}{N_{\text{eff}}}, \qquad (14)$$

where N_{eff} is given by Eq. (12). In the regime of low mass $\mu \ll \sqrt{\omega/Lq}$, it is equivalent to $\bar{P}_\gamma = P_\gamma$ and the mixing parameter oscillates as a function of the paraphoton mass. For higher masses, oscillations are smoothed to a mean value. Note that the relevant mass ranges concerning axionlike particles are situated in the low mass regime, which explains why the averaging over the laser bandwidth was not useful.

The deep gray area in Fig. 14 represents the parameters for a paraphoton that our measurements exclude with a 95% confidence level. It corresponds to a maximum photon regeneration probability $P_\gamma = 9.4 \times 10^{-24}$. This sets a limit $\chi < 1.1 \times 10^{-6}$ for $1 < \mu < 10$ meV [for higher masses, Eq. (6) is not valid anymore]. This improves by almost 1 order of magnitude the exclusion area obtained by the BFRT photon regeneration experiment [3]. The enhanced probability at $\mu = \omega$ given by Eq. (7) corresponds to $\chi < 1.9 \times 10^{-7}$. For other ranges of mass, a more complicated calculation is required [25] which is beyond the scope of this article. Nevertheless, comparing to other laboratory experiments [37,38] (see [39] for review), we
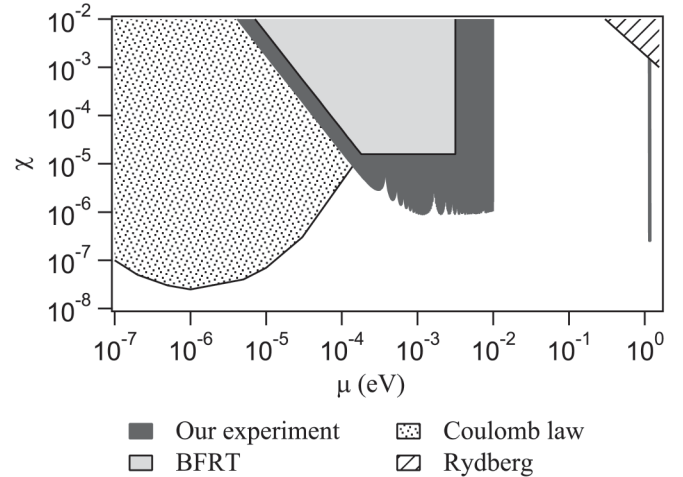

FIG. 14. 95% confidence level limits on photon-paraphoton mixing parameter as a function of the paraphoton mass obtained to our null result (deep gray area). Shaded regions are excluded. This is compared to excluded regions obtained by the BFRT photon regeneration experiment [3] (light gray area), to searches for deviations of the Coulomb law [37] (points) and to comparisons of the Rydberg constant for different atomic transitions [38] (stripes).

were able to constrain the paraphoton parameters in a region which had not been covered so far by purely terrestrial experiments.

VII. CONCLUSION AND OUTLOOKS

We have presented the final results of our photon regeneration experiment which exclude the PVLAS results. Our null measurement leads to limits similar to other purely terrestrial axion searches and improves the preceding limits by more than 1 order of magnitude concerning paraphotons [17].

As far as axionlike particles are concerned, improving the sensitivity of our apparatus in order to test the axion model predictions seems rather unrealistic, especially as the possible mass and two-photon coupling constant ranges are still several orders of magnitude wide. In that respect, magnetic birefringence experiments like the one presently under development in Toulouse [40] seem more promising: aimed at measuring for the first time the long predicted QED magnetic birefringence of vacuum [41], it will improve by 1 to 2 orders of magnitude the precision of purely terrestrial axion searches.

Generally speaking, let us argue that such precision optical experiments may prove useful for experimentally testing the numerous theories beyond the standard model in the low energy window, a range in which the large particle accelerators are totally helpless. For example, our apparatus can be modified to become sensitive to chameleon fields [42].

Finally, very intense laser beams such as those planned at ELI [43] will become available in the forthcoming years. Such facilities should open new exciting opportunities for our field.

[1] R. D. Peccei and H. R. Quinn, Phys. Rev. Lett. **38**, 1440 (1977); Phys. Rev. D **16**, 1791 (1977).
[2] S. Weinberg, Phys. Rev. Lett. **40**, 223 (1978); F. Wilczek, Phys. Rev. Lett. **40**, 279 (1978).
[3] R. Cameron *et al.*, Phys. Rev. D **47**, 3707 (1993).
[4] S. J. Asztalos *et al.*, Phys. Rev. D **69**, 011101(R) (2004); L. D. Duffy *et al.*, Phys. Rev. D **74**, 012006 (2006).
[5] S. Andriamonje *et al.* (CAST Collaboration), J. Cosmol. Astropart. Phys. 04 (2007) 010.
[6] For a review, see G. G. Raffelt, J. Phys. A **40**, 6607 (2007), and references therein.
[7] P. Sikivie, Phys. Rev. Lett. **51**, 1415 (1983); Phys. Rev. D **32**, 2988 (1985).
[8] E. Iacopini and E. Zavattini, Phys. Lett. **85B**, 151 (1979).
[9] L. Maiani, R. Petronzio, and E. Zavattini, Phys. Lett. B **175**, 359 (1986).
[10] K. Van Bibber *et al.*, Phys. Rev. Lett. **59**, 759 (1987).
[11] V. V. Popov and O. V. Vasil'ev, Europhys. Lett. **15**, 7 (1991).
[12] D. P. Woody and P. L. Richards, Phys. Rev. Lett. **42**, 925 (1979).
[13] H. Georgi, P. Ginsparg, and S. L. Glashow, Nature (London) **306**, 765 (1983); M. Axenides and R. Brandenberger, Phys. Lett. **134B**, 405 (1984).
[14] L. B. Okun, Zh. Eksp. Teor. Fiz. **83**, 892 (1982) [Sov. Phys. JETP **56**, 502 (1982)].
[15] J. C. Mather *et al.*, Astrophys. J. Lett. **354**, L37 (1990); H. P. Gush, M. Halpern, and E. H. Wishnow, Phys. Rev. Lett. **65**, 537 (1990).
[16] S. Abel and J. Santiago, J. Phys. G **30**, R83 (2004); R.
Blumenhagen *et al.*, Phys. Rep. **445**, 1 (2007).
[17] M. Ahlers *et al.*, Phys. Rev. D **76**, 115005 (2007).
[18] J. Jaeckel and A. Ringwald, Phys. Lett. B **659**, 509 (2008).
[19] M. Ahlers *et al.*, Phys. Rev. D **77**, 095001 (2008).
[20] P. De Bernardis *et al.*, Astrophys. J. **284**, L21 (1984).
[21] A. De Angelis and R. Pain, Mod. Phys. Lett. A **17**, 2491 (2002).
[22] E. Zavattini *et al.*, Phys. Rev. Lett. **96**, 110406 (2006); **99**, 129901 (2007).
[23] C. Robilliard *et al.*, Phys. Rev. Lett. **99**, 190403 (2007).
[24] G. Raffelt and L. Stodolsky, Phys. Rev. D **37**, 1237 (1988).
[25] S. L. Adler *et al.*, arXiv:0801.4739v4 [Ann. Phys. (to be published)].
[26] See http://www.luli.polytechnique.fr/pages/LULI2000. htm.
[27] J.-P. Zou *et al.*, Appl. Opt. **47**, 704 (2008).
[28] P. Frings *et al.*, Rev. Sci. Instrum. **77**, 063903 (2006).
[29] S. Batut *et al.*, IEEE Trans. Appl. Supercond. **18**, 600 (2008).
[30] A dark count, originating from electronic noise, corresponds to the apparent detection of a photon while no light strikes the detector.
[31] D. S. Bethune, W. P. Risk, and G. W. Pabst, J. Mod. Opt. **51**, 1359 (2004).
[32] The main advantage of using mirrors to strongly decrease the laser intensity instead of densities is to avoid thermal effects within the optics and thus to obtain a transmission independent on incident power.
[33] A. S. Chou *et al.*, Phys. Rev. Lett. **100**, 080402 (2008).
[34] E. Zavattini *et al.*, Phys. Rev. D **77**, 032006 (2008).

[35] S. DePanfilis *et al.*, Phys. Rev. Lett. **59**, 839 (1987); W. U. Wuensch *et al.*, Phys. Rev. D **40**, 3153 (1989).

[36] C. Hagmann *et al.*, Phys. Rev. D **42**, 1297 (1990).

[37] G. D. Cochran and P. A. Franken, Bull. Am. Phys. Soc. **13**, 1379 (1968); D. F. Bartlett, P. E. Goldhagen, and E. A. Phillips, Phys. Rev. D **2**, 483 (1970); E. R. Williams, J. E. Faller, and H. A Hill, Phys. Rev. Lett. **26**, 721 (1971).

[38] R. G. Beausoleil *et al.*, Phys. Rev. A **35**, 4878 (1987).

[39] D. F. Bartlett and S. Logl, Phys. Rev. Lett. **61**, 2285 (1988).

[40] R. Battesti *et al.*, Eur. Phys. J. D **46**, 323 (2008).

[41] H. Euler and K. Kochel, Naturwissenschaften **23**, 246 (1935); W. Heisenberg and H. Euler, Z. Phys. **98**, 714 (1936); Z. Bialynicka-Birula and I. Bialynicka-Birula, Phys. Rev. D **2**, 2341 (1970); S. L. Adler, Ann. Phys. (N.Y.) **67**, 599 (1971).

[42] P. Brax *et al.*, Phys. Rev. D **76**, 085010 (2007); M. Ahlers *et al.*, Phys. Rev. D **77**, 015018 (2008); H. Gies *et al.*, Phys. Rev. D **77**, 025016 (2008).

[43] http://www.extreme-light-infrastructure.eu.

[44] J. E. Kim, Phys. Rev. Lett. **43**, 103 (1979); M. A. Shifman, A. I. Vainshtein, and V. I. Zakharov, Nucl. Phys. **B166**, 493 (1980).

[45] M. Dine, W. Fischler, and M. Srednicki, Phys. Lett. **104B**, 199 (1981); A. P. Zhitnitskii, Sov. J. Nucl. Phys. **31**, 260 (1980).